Research Article

Abdulrahman B. M. Alzahrani*

Examining the role of activation energy and convective boundary conditions in nanofluid behavior of Couette-Poiseuille flow

https://doi.org/10.1515/phys-2023-0176
received August 17, 2023; accepted December 18, 2023

Abstract: This work investigates the behavior of a nanofluid in a horizontal channel under advection boundary conditions within the domain of magnetohydrodynamic radiative Couette-Poiseuille flow. We utilize the Haar wavelet collocation method (HWCM) to investigate the effects of energy activation. This research relies on the mathematical model introduced by Buongiorno, which effectively captures the flow dynamics and incorporates the influence of chemical processes. To streamline the governing flow equations, we employ boundary layer approximations. The HWCM is employed to numerically solve the non-linear coupled partial differential equations that regulate momentum, heat transport, and mass transfer processes. We examine the impact of several dimensionless convergence parameters on the velocity, temperature, and concentration profiles and give visual representations of these results. It is crucial to highlight that the activation energy of the specific chemical reaction is directly linked to the concentration of nanoparticles. The effect of Brownian motion on nanoparticle concentration varies from that of the thermophoresis parameter.

Keywords: Couette-Poiseuille flow, Haar wavelet collocation method, energy and convective boundary conditions

Nomenclature

A	reaction rate
Bi	Biot number
Br	Brinkman number
C_f	skin fraction
C_s	heat capacity (J kg^{-1} K)
E	activation energy
N_b	Brownian motion parameter
N_j	convection diffusion parameter
N_r	buoyancy ratio
Nu	Nusselt number
Rd	radiation parameter
Re	Reynolds number
Sc	Schmidt number
Sh	Sherwood number

Greek symbols

μ	dynamic viscosity (N s m^{-2})
$(\rho C_p)_f$	heat capacity of the base fluid (J K^{-1} m^{-3})
ε	momentum accommodation coefficient
α	thermal diffusivity $\frac{k}{(\rho C)_f}$(m^2 s^{-1})
β	volumetric volume expansion coefficient (K^{-1})
τ	parameter defined by $\frac{(\rho C_p)_s}{(\rho C_n)}$
ν	kinematic viscosity (m^2 s^{-1})
ϑ	dimensionless temperature
ϕ	nanoparticle concentration
σ^*	Stefan–Boltzmann constant
σ	electrical conductivity (S m^{-1})
Y	temperature

1 Introduction

Nanofluids, which involve the suspension of nanoscale particles within a convective heat transfer fluid, represent a fascinating scientific frontier where the intricate interplay of thermodynamic forces and fluid dynamics is pivotal in enhancing thermal conductivity. Numerous strategies have been developed to augment the thermal conductivity of these fluids through the dispersion of nano- and micro-scale elements within the liquid matrix. Extensive research has established that including trace amounts of metallic oxide

* Corresponding author: Abdulrahman B. M. Alzahrani, Department of Mathematics, College of Science, King Saud University, P.O. Box 2455, Riyadh, 11451, Saudi Arabia, e-mail: aalzahranii@ksu.edu.sa

nanoparticles significantly enhances thermal conductivity [1–3]. Additionally, the study of natural convection in nanofluids has garnered attention in recent years [4,5], with investigations of natural convective boundary-layer flows across vertical plates, as studied by Kuznetsov and Nield [6] using the Buongiorno model [7]. Boundary flows in porous media with convection dominance, as explored by Wang *et al.* [8]. Detailed insights into nanofluid flow properties and convective heat transfer are provided in previous literature [9–13].

Moreover, the scientific community has shown significant interest in studying convective heat transfer and magnetohydrodynamic (MHD) motion at the nanofluid interface, focusing on potential applications across various sectors. The peristaltic transport of micro-polar fluids in channels featuring convective boundary conditions and heat source/sink effects has been explored, yielding exact solutions [14,15]. Studies investigating the combined impact of Hall and convective conditions on the peristaltic flow of couple-stress fluids in asymmetric, slanted channels have been conducted, advocating the utilization of peristaltic fluid flow in engineering contexts, incorporating Hall current, thermal deposition, and convective conditions [16,17]. Hayat *et al.* analyzed mixed convection and varying thermal conductivity in viscoelastic fluids [18]. Further studies have investigated the effects of two-fold stratification and mixed convection in magneto-Maxwell nanofluids [19,20] and the MHD slip flow of micro-polar liquids due to vertically contracting surfaces. The convective flow of Maxwell liquids with thermal radiation was explored by Hayat *et al.* [21], shedding light on the dynamic alterations experienced by electric fluids moving through magnetic fields created by external sources. Rana *et al.* [22] researched natural convection flows of carbon nanotube nanofluids featuring Prabhakar-like thermal transfer characteristics. Additionally, Lou *et al.* [23] investigated the effects of Coriolis force on the dynamics of spinning micropolar dusty fluids under considerable Lorentz force.

The Arrhenius activation energy and mass transfer analysis procedure have received significant attention owing to their relevance in chemical engineering, nuclear reactor cooling, geothermal reservoirs, and thermal oil recovery. This approach allows for an in-depth examination of the intricate relationships between chemical reactions and mass movement, considering various reactant species and production rates. Several studies [24–31] have contributed to a better understanding of nanomaterials enhancing thermal conductivity and thermal performance. Bestman [32] employed activation energy kinetics analysis to investigate convection-driven mass transport in a vertical conduit filled with porous material, employing a perturbation approach to find an analytical solution. Maleque investigated natural convection in a binary chemical reaction system [33]. Mustafa *et al.* [34] discussed how buoyancy influences a magneto-nanofluid's chemical reactions and activation energy as it flows across a vertical surface.

Researchers have converged on several key findings: the effects of the thermophoresis parameter on nanoparticle concentration are contrary to those of Brownian motion, and nanoparticle concentration is directly proportional to activation energy and the rate of chemical reaction. Mohyud-Din *et al.* [35] examined the outcomes of MHD flow in both convergent and divergent channels, concluding that nanoparticle distribution has a diminishing influence as the Reynolds number increases in a divergent channel. Still, it exerts an increasing effect in a converging channel. Previous studies [36,37] considered the flow through a rotating frame with an elastic surface and a binary chemical reaction, expanding our understanding of this complex field. It is of great scientific interest to investigate and assess the activation of energy and thermal dynamics in the context of manufacturing extrusion, considering the impact of radiation phenomena because of the work of some of the above researchers and its applicability in a wide range of scientific and technological disciplines. The Buongiorno fluid model introduces innovative features by considering solid fraction, thermophoresis, Brownian motion, effective thermal conductivity, changeable properties, and non-uniform heat sources. These combined characteristics improve its precision and usefulness in simulating the behavior of nanofluids and heat transfer, making it a valuable tool in multiple scientific and technical fields. This study presents a new method that utilizes similarity transformations to reorganize the partial differential equations efficiently. The transformed equations are then effectively handled using the Haar Wavelet Collocation method (HWCM) [38–40]. This method effectively deals with the intricate network of interconnected differential equations that govern the system, a unique aspect of our research. A schematic flow chart of the proposed approach is given in Scheme 1.

An overview of this work is as follows. Section 2 begins by providing the flow geometry in our current study. The methodology and the non-linear coupled partial differential equations describing momentum, heat transfer, and mass transfer phenomena numerically solved using the HWCM are provided in Sections 3 and 4, along with results and discussion. Finally, Section 5 contains the conclusion of our study.

2 Flow geometry

Two indefinitely long parallel plates are separated by distance ($2d$), creating a confined zone through which an

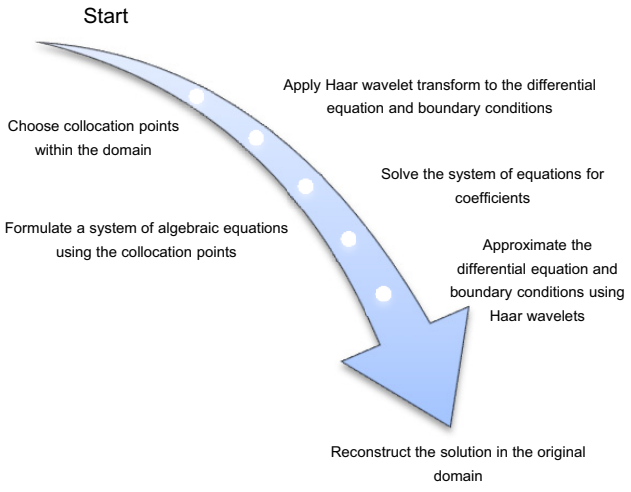

Scheme 1: A schematic flow chart of the proposed approach.

incompressible fluid flows continuously. Assume the upper plate moves at a constant velocity ($\overline{U}$), with the bottom plate at temperature (t_1) and the higher plate at temperature (t_2). Assuming an orthogonal coordinate system (x, y), with the plates at $y = -d$ and ($y = d$), the y-axis would represent the orthogonal direction concerning the plates. At the same time, the x-axis would be the direction of fluid flow, while the y-axis runs counter to the direction of the gravitational acceleration vector (g) and is perpendicular to the channel. The channel wall's bottom and top must satisfy the convective boundary criteria (Figure 1).

The fluid is y-electrically transmitted through a non-uniform magnetic field (b). The electric field and Hall current are considered insignificant at low Reynolds numbers. In this scenario, it is assumed that the nanofluid's physical properties are always the same. The fundamental equations for an incompressible fluid, including momentum, mass, and energy conservation, are as follows [41]:

$$\frac{\partial u}{\partial x} + \frac{\partial v}{\partial y} = 0, \tag{1}$$

$$\rho_f.\,(u.\,\nabla)u = -\nabla P + \mu\nabla^2 u + g(C\rho_s + \rho_f[(1-\beta)(T - T_\circ)(1-C)]) + j \times b, \tag{2}$$

$$\rho_f C(u.\,\nabla)T = (\nabla^2 T)k + \rho_s C\left\{\left(\frac{D_T}{T_\circ}\right)(\nabla T)^2 + D_b(\nabla C.\,[\nabla T])\right\} + \Theta - \nabla.\,Q_r + \frac{1}{\sigma}(j \times j), \tag{3}$$

$$\rho_s.\,(u \times \nabla)C = -\nabla \times j_s - \rho_s K^2\left(\frac{T}{T_\circ}\right)^m (C - C_\circ)e^{\frac{E_a}{\kappa T}}. \tag{4}$$

Here mass flux, magnetic field, current density, and gravitational acceleration are defined as [42],

$$j_s = -\rho_s\left[D_b\nabla C + \left(\frac{D_T}{T_\circ}\right)\nabla T\right], b = (0, b_\circ, 0), \quad j = \sigma(u \times b), g = (0, g_\circ, 0). \tag{5}$$

The exponential term in Eq. (4) represents the activation energy in a chemical process [43], where Boltzmann and fitted rate constants are defined by (m) and (κ). Thus, the fields of Eqs. (1)–(4) can be broken down into their constituent parts along with boundary conditions [44]:

$$\frac{\partial u_1}{\partial x} + \frac{\partial u_2}{\partial y} = 0, \tag{6}$$

$$\frac{\partial P}{\partial x} = \mu\frac{\partial^2 u_1}{\partial y^2} - \sigma b_\circ^2 u_1 + g\left(\begin{matrix}(C - C_\circ)(\rho_s - \rho_f) \\ + \rho_f\beta(1 - C_\circ)(T - T_\circ)\end{matrix}\right), \tag{7}$$

$$u_1\frac{\partial T}{\partial x} = \frac{\partial^2 T}{\partial y^2} + \tau\left\{\frac{D_T}{T_\circ}\left(\frac{\partial T}{\partial y}\right)^2 + D_b\frac{\partial C}{\partial y}\frac{\partial T}{\partial y}\right\} + \frac{\mu}{(\rho C_p)_f}\left(\frac{\partial u}{\partial y}\right)^2 + \frac{\sigma b_\circ^2 u_1^2}{(\rho C_p)_f} - \frac{1}{(\rho C_p)_f}\frac{\partial q_r}{\partial y}, \tag{8}$$

$$-D_b\frac{\partial^2 C}{\partial y^2} = \frac{D_T}{T_\circ}\left(\frac{\partial T}{\partial y}\right)^2 - K_r^2\left(\frac{T}{T_\circ}\right)^m (C - C_\circ)e^{\frac{E_a}{\kappa T}}, \tag{9}$$

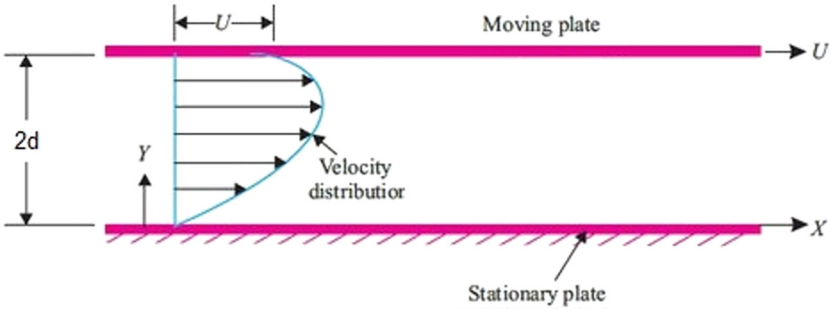

Figure 1: Flow diagram.

$$
\begin{aligned}
&u_1 = \bar{U},\ u_2 = 0,\ [t_2 - T]h_{\mathrm{f}} = -k\left(\frac{\partial T}{\partial y}\right),\\
&[c_2 - C]h_{\mathrm{s}} = -D_{\mathrm{b}}\frac{\partial C}{\partial y},\ y = d.\\
&u_1 = 0,\ u_2 = 0,\ [t_1 - T]h_{\mathrm{f}} = -k\frac{\partial T}{\partial y},\\
&[c_1 - C]h_{\mathrm{s}} = -D_{\mathrm{b}}\frac{\partial C}{\partial y},\ y = -d.
\end{aligned}
\tag{10}
$$

By defining dimensionless parameters [45], one can transform the above system into a non-dimension form

$$
\begin{aligned}
&\xi = \frac{x}{a},\ F = \frac{u_1}{a},\ \vartheta = \frac{T - T_\circ}{t_1 - T_\circ},\ p = \frac{a^2 P}{\mu U_{m_1}},\ n_1 = \frac{t_2 - T_\circ}{t_1 - T_\circ},\\
&\zeta = \frac{y}{a}, G = \frac{u_2}{a},\ \phi = \frac{C - C_\circ}{c_1 - C_\circ},\ U = \frac{\bar{U}}{U_{m_1}},\ m_1 = \frac{c_2 - C_\circ}{c_1 - C_\circ}.
\end{aligned}
\tag{11}
$$

Since the stream's path lies along the x-axis, the y-axis velocity component must be null, *i.e.*, the steady pressure difference drives the fluid movement. The maximum speed (U_{m_1}) was assumed to have happened between the two walls. In this situation, we ignore the temperature and concentration scales (m_1) entirely. For this case, the Rosseland approximation describes the radiative heat flux $q_{\mathrm{r}} = \frac{16T_\circ^3\sigma}{3k_\circ}\frac{\partial T}{\partial y}$.

$$
\frac{\partial^2 F}{\partial \zeta^2} - M^2 F + \frac{R_{\mathrm{a}}}{R_{\mathrm{e}} pr}(\vartheta - N_{\mathrm{r}}\phi) - p = 0, \tag{12}
$$

$$
\begin{aligned}
&(1 + R_{\mathrm{d}})\frac{\partial^2 \vartheta}{\partial \zeta^2} + N_{\mathrm{b}}\frac{\partial \vartheta}{\partial \zeta}\frac{\partial \phi}{\partial \zeta} + N_{\mathrm{t}}\left(\frac{\partial \vartheta}{\partial \zeta}\right)^2 + B_{\mathrm{r}}\left(\frac{\partial F}{\partial \zeta}\right)^2\\
&+ M^2 B_{\mathrm{r}} F^2 - \lambda F(\zeta),
\end{aligned}
\tag{13}
$$

$$
\frac{\partial^2 \phi}{\partial \zeta^2} + \frac{N_{\mathrm{t}}}{N_{\mathrm{b}}}\frac{\partial^2 \vartheta}{\partial \zeta^2} - \mathrm{Sc} R_{\mathrm{e}} A(1 + \alpha\vartheta)^m e^{-\frac{\Upsilon}{1+\alpha\vartheta}}, \tag{14}
$$

with boundary conditions,

$$
\begin{aligned}
&F(1) = U,\ \vartheta'(1) = -B_{\mathrm{i}}(n_1 - \vartheta(1)),\\
&\phi'(1) = -N_{\mathrm{j}}(m_1 - \phi(1)),\\
&F(-1) = 0\ ,\ \vartheta'(-1) = -B_{\mathrm{i}}(1 - \vartheta(-1)),\\
&\phi'(-1) = -N_{\mathrm{j}}(1 - \phi(-1)),
\end{aligned}
\tag{15}
$$

where

$$
\begin{aligned}
&R_{\mathrm{a}} = \frac{(1 - C_\circ)(t_1 - T_\circ)}{\nu\alpha},\ M^2 = \frac{\sigma b_\circ^2 a^2}{\mu},\ R_{\mathrm{e}} = \frac{aU_m}{\nu},\\
&\nu = \frac{\mu}{\rho},\ \mathrm{pr} = \frac{\nu}{\alpha},\\
&A = \frac{K_{\mathrm{r}}^2 a}{U_{\mathrm{m}}}, B_{\mathrm{r}} = \frac{\mu U_{\mathrm{m}}^2}{k(t_1 - T_\circ)},\ N_{\mathrm{b}} = \frac{\tau D_{\mathrm{b}}(c_1 - C_\circ)}{\alpha},\\
&N_{\mathrm{t}} = \frac{\tau D_{\mathrm{t}}(t_1 - T_\circ)}{\alpha T_\circ},\\
&N_{\mathrm{r}} = \frac{(\rho_{\mathrm{p}} - \rho_{\mathrm{f}})(c_1 - C_\circ)}{\rho_{\mathrm{f}}\beta(1 - C_\circ)(t_1 - T_\circ)}, R_{\mathrm{d}} = \frac{16\sigma t_1^3}{3k_\circ k},\ \mathrm{Sc} = \frac{\nu}{D_{\mathrm{b}}},\\
&\alpha = \frac{(t_1 - T_\circ)}{T_\circ},\\
&\Upsilon = \frac{E_{\mathrm{a}}}{\kappa T_\circ},\ B_{\mathrm{i}} = \frac{kh_{\mathrm{f}}}{a},\ N_{\mathrm{j}} = \frac{ah_{\mathrm{s}}}{D_{\mathrm{b}}}.
\end{aligned}
\tag{16}
$$

3 Methodology

Assuming that A and B are constants, then $\zeta \in [A, B]$, the ith Haar wavelet family is defined as

$$
H_i(\zeta) = \begin{cases} 1 \text{ for } \zeta \in [a_1, b_1) \\ -1 \text{ for } \zeta \in [b_1, c_1) \\ 0 \text{ elsewhere,} \end{cases} \tag{17}
$$

with

$$
a_1 = k/\bar{m}_1,\ b_1 = (k + 1)/2/\bar{m}_1,\ c_1 = k + 1/\bar{m}_1, \tag{18}
$$

where $\bar{m}_1 = 2^j$ is the highest attainable resolution, we will refer to this quantity as $\bar{M} = 2j$, each of the $2\bar{M}$ subintervals of the interval $[A, B]$ has a length $\zeta = (B, A)/2\bar{M}$, where $\bar{M}$ is the number of subintervals($2\bar{M}$), a translation parameter $k = 0,\ 1,\ \ldots,\ \bar{m}_1 - 1$ and a dilatation parameter $j = 0,\ 1,\ \ldots, J$. The formula for the wavelet number i is $i = \bar{m}_1 + k + 1$.

For Haar function and their integrals

$$
p_{i1}(\zeta) = \int_0^\zeta H_i(\zeta), \tag{19}
$$

$$
p_{i,\,l+1}(x) = \int_0^\zeta p_{i,l}(\zeta)\,\mathrm{d}\zeta,\ l = 1,\ 2,\ \ldots, \tag{20}
$$

To calculate these integrals, we use Eq. (17)

$$p_{i1}(\zeta) = \begin{cases} \zeta - a_1 & \text{for } \zeta \in [a_1, b_1) \\ c_1 - \zeta & \text{for } \zeta \in [b_1, c_1) \\ 0 & \text{elsewhere,} \end{cases} \tag{21}$$

$$p_{i2}(\zeta) = \begin{cases} \frac{1}{2}(\zeta - a_1)^2 \text{ for } \zeta \in [a_1, b_1) \\ \frac{1}{4\bar{m}_1^2} - \frac{1}{2}(c_1 - \zeta)^2 \text{ for } \zeta \in [b_1, c_1) \\ \frac{1}{4\bar{m}_1^2} \text{ for } \zeta \in [c_1, 1) \\ 0 \text{ elsewhere,} \end{cases} \tag{22}$$

$$p_{i3}(\zeta) = \begin{cases} \frac{1}{6}(\zeta - a_1)^3 \text{ for } \zeta \in [a_1, b_1) \\ \frac{1}{4\bar{m}_1^2}(\zeta - b_1) - \frac{1}{6}(c_1 - \zeta)^3 \text{ for } \zeta \in [b_1, c_1) \\ \frac{1}{4\bar{m}_1^2}(\zeta - \beta) \text{ for } \zeta \in [c_1, 1) \\ 0 \text{ elsewhere,} \end{cases} \tag{23}$$

We also present the notation shown below.

$$C_{i1} = \int_0^L p_{i1}(\zeta)\mathrm{d}\zeta, \tag{24}$$

$$C_{i2} = \int_0^L H_i(\zeta)\mathrm{d}\zeta. \tag{25}$$

Summation of the Haar wavelet function can be written as follows:

$$F(\zeta) = \sum_{i=1}^{\infty} a_i H_i(\zeta). \tag{26}$$

We may approximate the highest order derivatives of F, ϑ, and ϕ given for the problems (12)–(14) to build a straightforward and precise HWCM.

$$F''(\zeta) = \sum_{i=1}^{2M} a_i H_i(\zeta), \tag{27}$$

$$\vartheta''(\zeta) = \sum_{i=1}^{2M} b_i H_i(\zeta), \tag{28}$$

$$\phi''(\zeta) = \sum_{i=1}^{2M} c_i H_i(\zeta). \tag{29}$$

Integrating Eqs (27–29), we obtain the values $F''(\zeta)$, $F'(\zeta)$ and $F(\zeta)$, respectively,

$$F''(\zeta) = \sum_{i=1}^{2M} a_i \left(p_{i,1}(\zeta) - \frac{1}{\hat{L}} C_{i,1} \right), \tag{30}$$

$$F'(\zeta) = \sum_{i=1}^{2M} a_i \left(p_{i,2}(\zeta) - \frac{1}{\hat{L}} \zeta C_{i,1} \right), \tag{31}$$

Table 1: HWCM convergence, when $m_1 = n_1 = 0, U = \Upsilon = \alpha = A = R_d = B_r = 1$, $m = 0.5$, Sc = 10, $M = 2$, and $\lambda = 2$, $N_t = N_r = N_j = B_i = 0.5$, $R_e = 0.3$, $N_b = 0.5$

Order of approximation	Time	$-F'(\zeta)$	$-\vartheta'(\zeta)$	$-\phi'(\zeta)$
1	3.45319	0.3688	1.0003	0.8873
5	25.84384	0.3681	0.9991	0.8865
11	64.2033	0.3673	0.9982	0.8857
18	147.7525	0.3674	0.9934	0.8849
22	214.2009	0.3657	0.9908	0.8846
25	380.2949	0.3652	0.9900	0.8838

$$F(\zeta) = \sum_{i=1}^{2M} a_i \left(p_{i,3}(\zeta) - \frac{1}{\hat{L}} \frac{\zeta^2}{2} C_{i,1} \right). \tag{32}$$

Assume $\hat{L}$ is a large number. A numerical solution for the ODEs is obtained by substituting Eqs (27)–(32) in Eqs (12)–(14) (Table 1).

In the next section, we can see a visual representation of the results of the proposed solution.

4 Results and discussion

This section used the HWCM to numerically solve the transformed non-linear differential Eqs (12)–(14) associated with the convective boundary conditions (15) from Figures 2–15, we discuss the effects of various evolving parameters on the

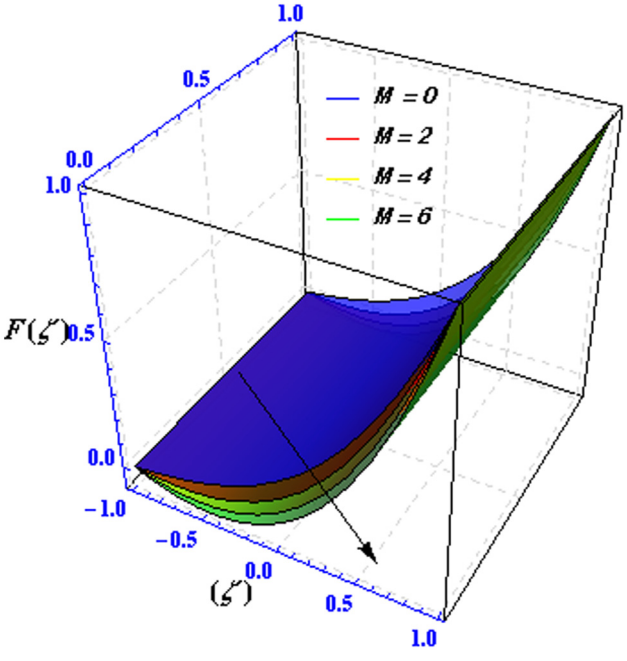

Figure 2: Evolution of $F(\zeta)$ for the spatial parameter (M).

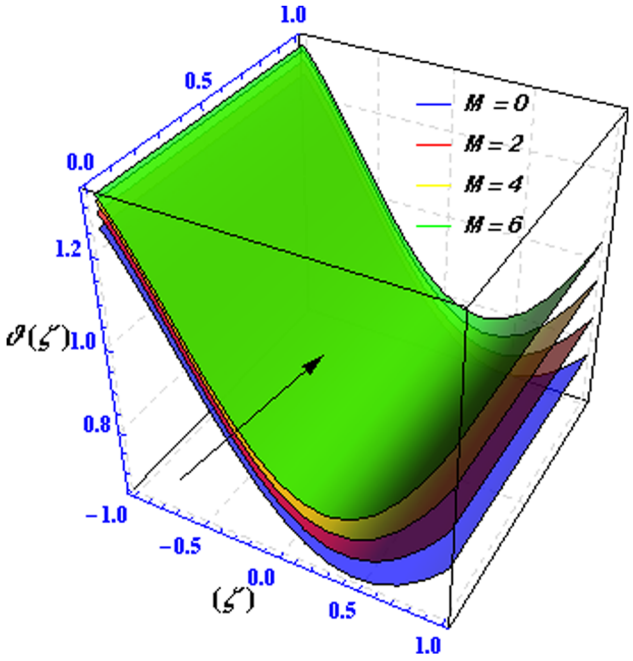

Figure 3: Evolution of $\vartheta(\zeta)$ for the spatial parameter (M).

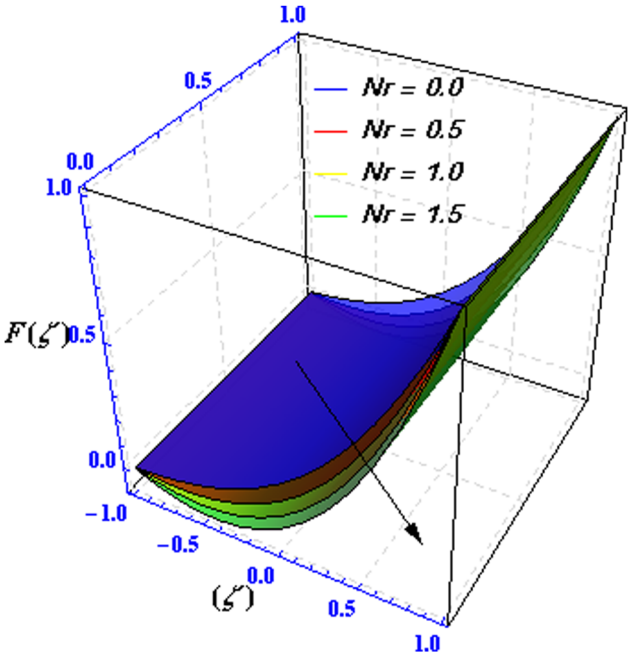

Figure 5: Evolution of $F(\zeta)$ for the spatial parameter (N_r).

flow field. The following analysis and outcomes are achieved by selecting suitable values for emerging parameters:

$m_1 = n_1 = 0,\ U = \Upsilon = \alpha = A = R_d = B_r = 1,$
$m = N_b = N_t = 0.5,$
$N_r = N_j = B_i = 0.5,\ R_e = 0.3,\ \mathrm{Sc} = 10,\ M = 2,$ and $\lambda = 2.$

The combined effect of the magnetic parameter (M) on the velocity, temperature, and concentration fields is shown in Figures 2–4. The phenomenon of hydromagnetic flow corresponds to $(M = 0)$, while that of hydrodynamic flow is led by $(M > 0)$. Figure 2 depicts a noticeable reduction in nanofluid flow velocity with its increase, attributed to the

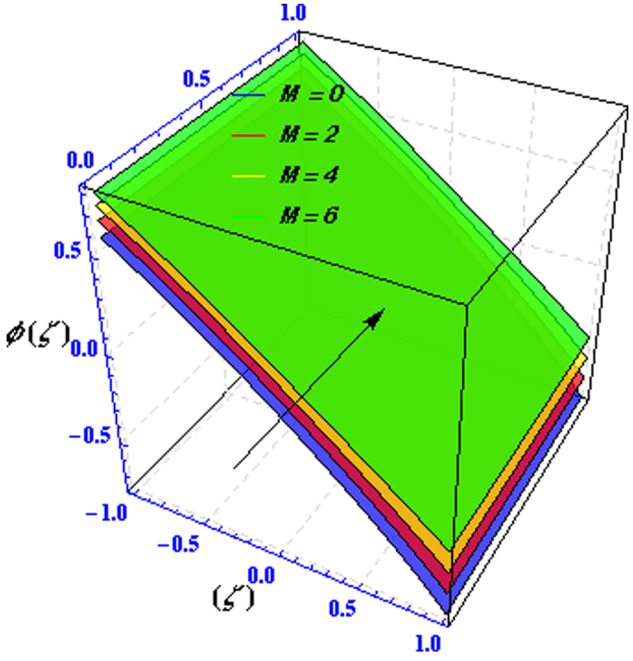

Figure 4: Evolution of $\phi(\zeta)$ for the spatial parameter (M).

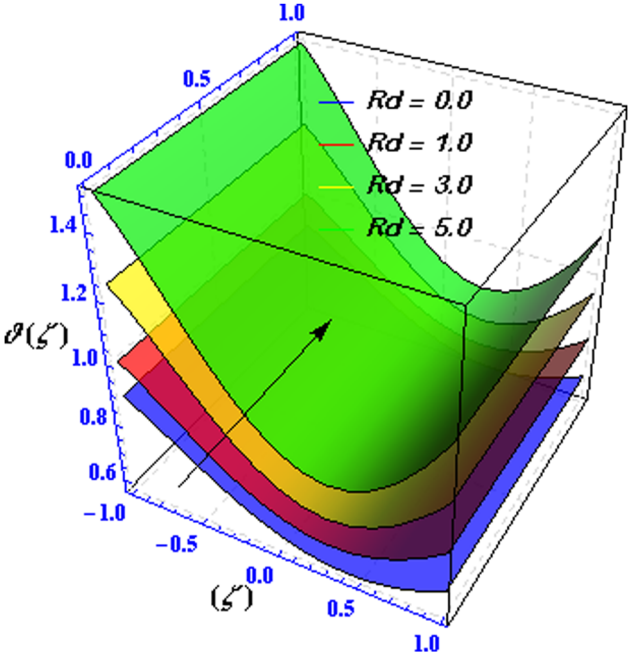

Figure 6: Evolution of $\vartheta(\zeta)$ for the spatial parameter (R_d).

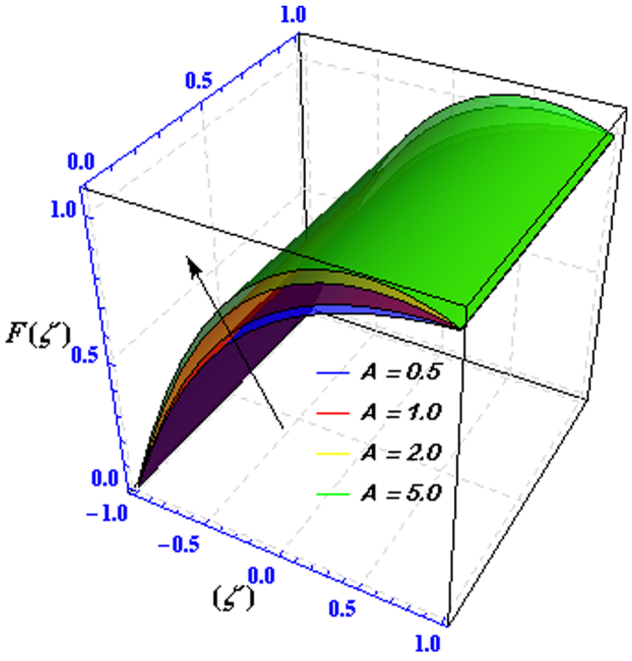

Figure 7: Evolution of $F(\zeta)$ concerning the spatial parameter (A).

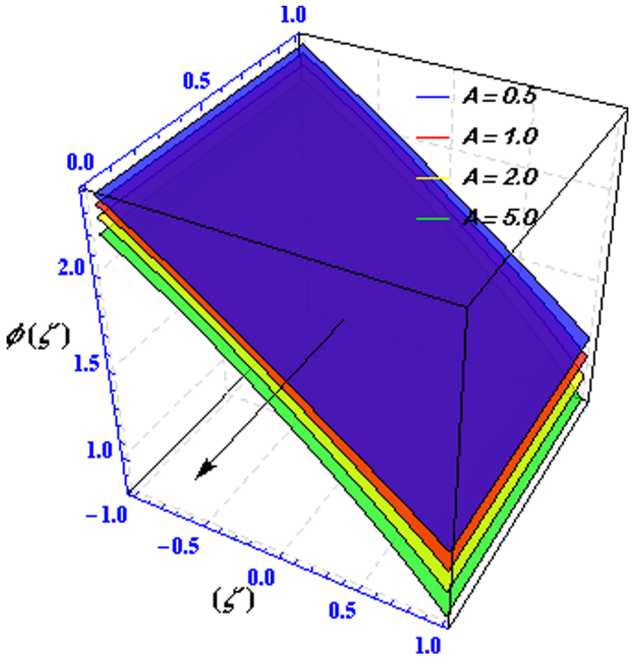

Figure 9: Evolution of $\phi(\zeta)$ to the spatial parameter (A).

amplification of opposing Lorentz forces acting on it. This phenomenon illustrates that as the flow of the nanofluid intensifies, the resistance it encounters from the Lorentz forces proportionally augments, resulting in the observed slowdown. Compared to the hydrodynamic flow, a more uniform temperature distribution characterizes hydromagnetic flow. The Lorentz force exerts more effect in a strong magnetic field. Figure 3 displays the enhanced temperature distribution resulting from the amplified Lorentz force, demonstrating a more uniform and effective thermal profile throughout the system. The increased distribution of temperature not only facilitates more efficient dissipation of heat but also reduces the presence of temperature gradients, enhancing the system's overall performance.

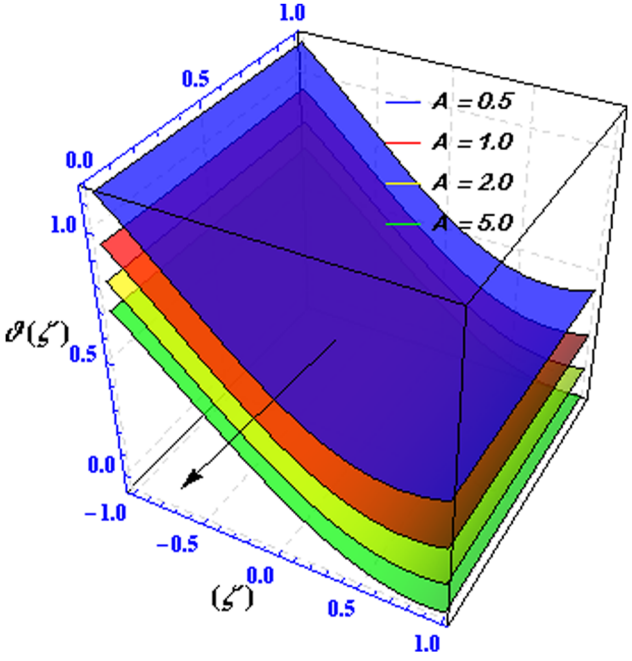

Figure 8: Evolution of $\vartheta(\zeta)$ for the spatial parameter (A).

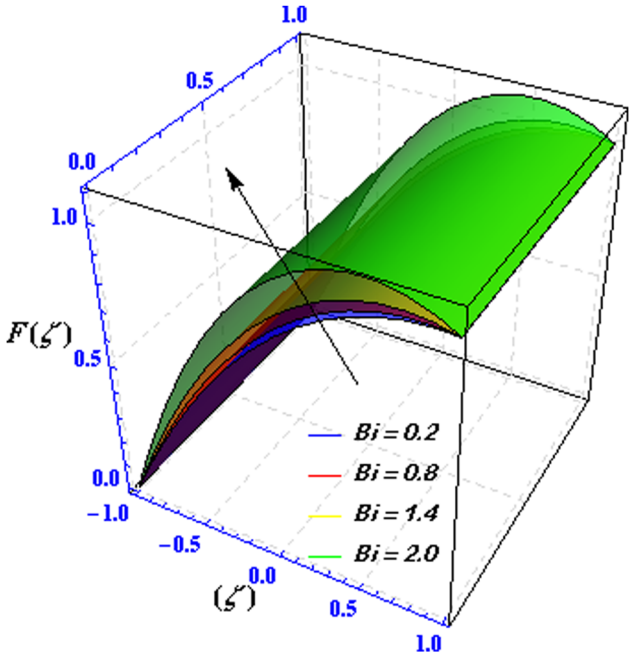

Figure 10: Evolution of $F(\zeta)$ concerning the spatial parameter (B_{i}).

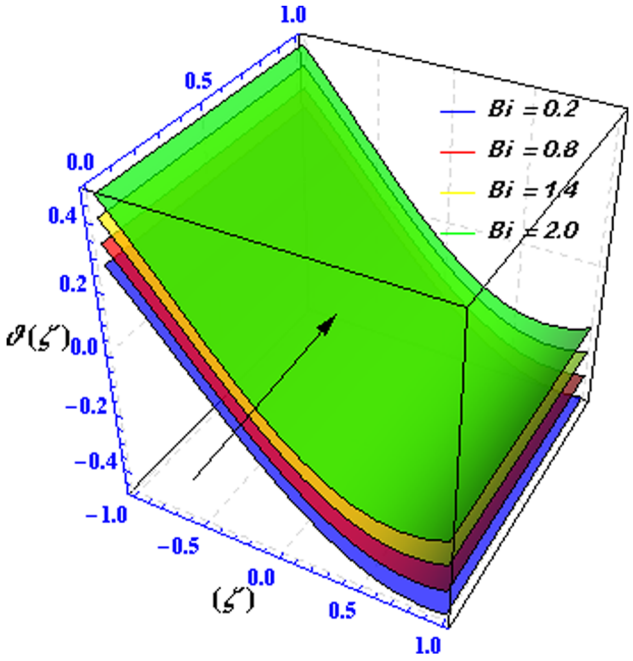

Figure 11: Evolution of $\vartheta(\zeta)$ concerning the spatial parameter (B_i).

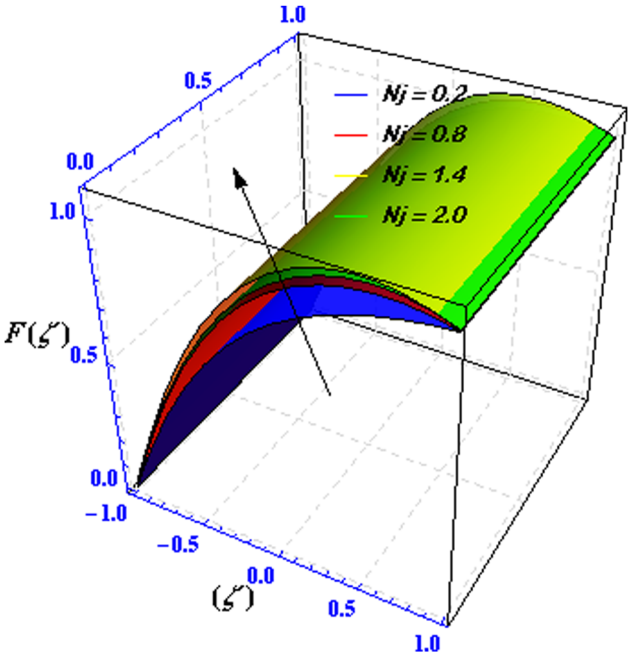

Figure 13: Evolution of $F(\zeta)$ concerning the spatial parameter (N_j).

Shifting our focus to Figure 4, the concentration curve is depicted in correlation with different magnetic field parameter values. The observed concentration profile demonstrates a clear positive correlation, indicating that a proportional increase in the concentration of the targeted compounds within the system accompanies an increase in the magnetic field parameter. This occurrence underscores the significant association between the intensity of the magnetic field (M) and the concentration of the desired components, indicating the possibility of meticulous regulation and enhancement of these processes.

Higher values of (N_r) seen in Figure 5 also influence the fluid motion. The drop in velocity profile directly results from the increase in opposite bouncing due to the

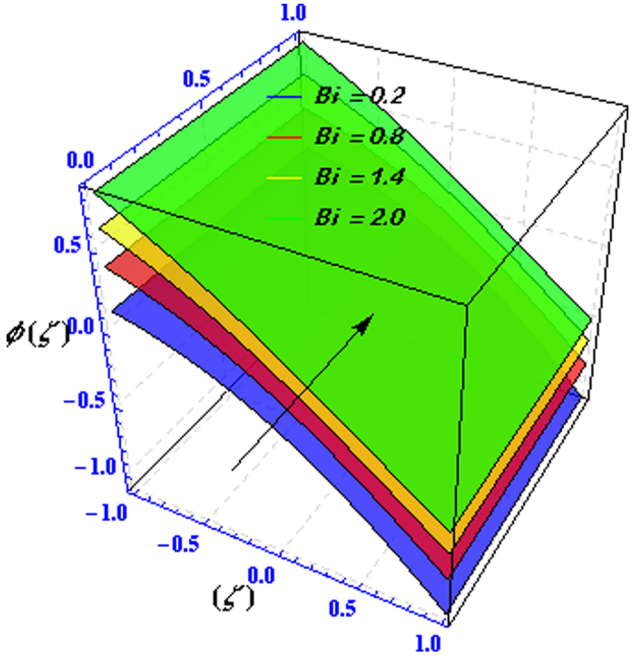

Figure 12: Evolution of $\phi(\zeta)$ concerning the spatial parameter (B_i).

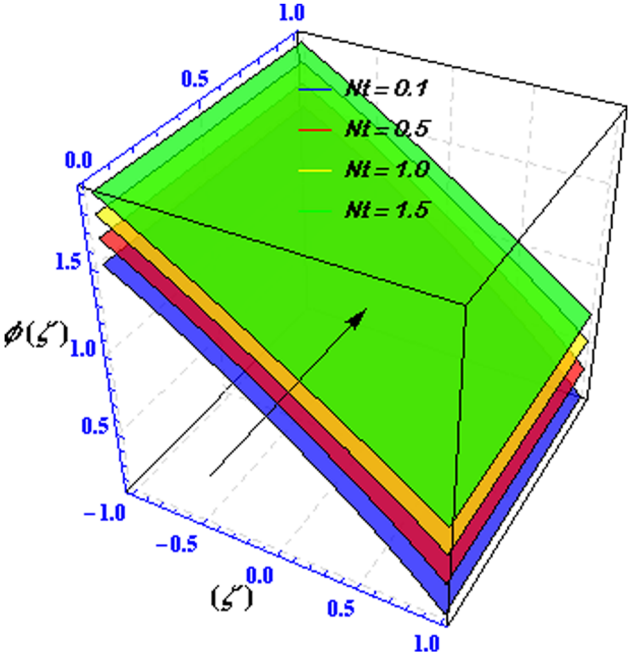

Figure 14: Evolution of $\phi(\zeta)$ concerning the spatial parameter (N_t).

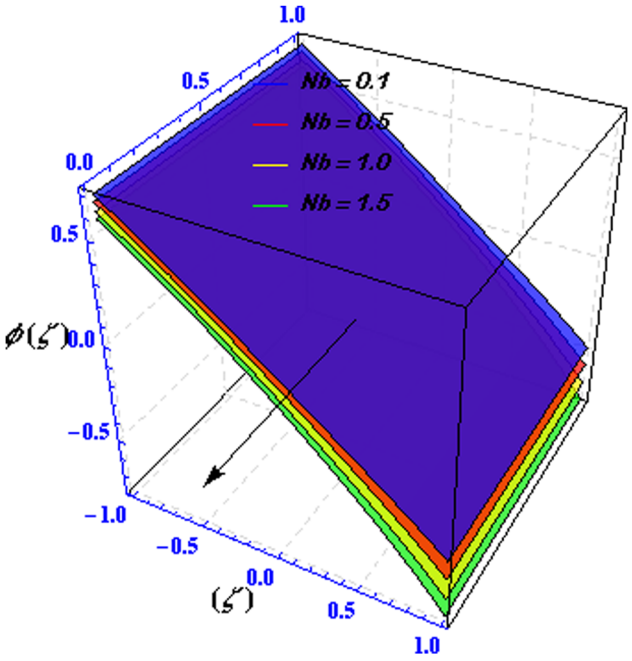

Figure 15: Evolution of $\phi(\zeta)$ concerning the spatial parameter (N_b).

Table 3: Nusselt number for different values of M, N_t, R_d, N_b and B_r.

(M)	(N_t)	(R_d)	(N_b)	(B_r)	$\vartheta'(-1)$	$\vartheta'(1)$
0.0	0.5	11	0.5	1	0.492929	0.504004
2.0					0.493246	0.504333
4.0					0.493493	0.504745
6.0					0.493810	0.505321
	0.5				0.493246	0.504333
	1.0				0.494116	0.506943
	1.5				0.494990	0.509565
	2.0				0.495869	0.512199
		1			0.493246	0.504333
		2			0.493262	0.504369
		3			0.493278	0.504406
		4			0.493293	0.504442
			0.5		0.493246	0.504333
			1.0		0.493848	0.506208
			1.5		0.494451	0.508085
			2.0		0.495055	0.509964
				0	0.492212	0.501538
				1	0.493246	0.504333
				5	0.494280	0.507129
				7	0.495314	0.509924

ambient nanoparticle volume percentage. The effect of the radiation parameter (R_d) on the temperature distribution is seen in Figure 6. As the radiation parameter increases, a more significant impact is seen on the nanofluid's temperature distribution. The physical mechanism underpinning this remarkable improvement is increased radiative energy transfer within the nanofluidic channel.

The velocity, temperature, and concentration profiles for various values of the chemical reaction parameter (A) are depicted in Figures 7–9, respectively. A steeper velocity profile may be observed as the chemical reaction parameter is raised. The chemical reaction causes a decrease in physical velocity, yet the velocity at the surface increases to its maximum value compared to the surface boundary.

Table 2: Skin friction coefficient for different values of M, N_r, Ra and Pr.

(M)	(N_r)	(Ra)	(P_r)	$-F'(-1)$	$-F'(1)$
0.0	0.5	2	7	−0.004573	0.004745
2.0				−0.004044	0.004606
4.0				−0.003453	0.004187
6.0				−0.002801	0.003489
	0.5			−0.004044	0.004606
	1.0			−0.004251	0.005911
	1.5			−0.004457	0.007216
	2.0			−0.004664	0.008522
		1		−0.005388	0.006848
		2		−0.004044	0.004606
		3		−0.002700	0.002364
		4		−0.001356	0.000122
			7	−0.004044	0.004606
			8	−0.004380	0.005166
			9	−0.004642	0.005602
			10	−0.004851	0.005951

Table 4: Sherwood number for different values of M, N_t, R_d, N_b and B_r.

(A)	(E)	(n_1)	(Y)	(Sc)	(R_d)	$-\phi'(-1)$	$-\phi'(1)$
0.0	2.0			10.0	1.0	−0.744148	2.330771
1.0						−0.870893	2.552822
2.0						−1.007160	2.795660
5.0						−1.153320	3.060250
	0.0					−0.124560	1.082631
	1.0					−0.241022	1.606220
	2.0					−0.870893	2.552820
	3.0					−1.842190	4.057940
		−1.0				−3.411570	6.359712
		0.0				−1.512590	3.509851
		0.5				−0.870893	2.552823
		1.0				−0.397690	1.851932
	1.0		0.0		0.5	0.052703	0.356023
	1.0		1.0			0.409739	0.715164
	1.0		2.0			2.652001	2.867631
	1.0		3.0			9.993070	9.019430
	1.0			1.0		5.312660	2.974801
	1.0			3.0		6.700660	4.696381
	1.0			5.0		8.257800	6.704832
	1.0			10.0		9.993070	9.019430

The velocity of the fluid decreases when the chemical reaction parameter, (A), is more significant than zero. The nanofluid's temperature and the nanoparticle volume concentration decrease with the increase in (A). This behavior indicates the diminutive impact of buoyant force owing to the concentration gradient on the concentration profile.

As shown in Figure 10, the peak velocity is modest regardless of the Biot number (Bi=0). Thermal resistance of the plate decreases as the convection Biot number rises. As a result, both the peak velocity and surrounding velocities increase substantially. In Figure 11, we can see how the temperature changes as a function of the Biot number (Bi) (the convection conduction parameter) since (Bi) is linked to convective cooling at the surface. Improving the thermal boundary layer due to a rise in (Bi) temperature leads to a rise. The concentration field as a function of the Biot number (Bi) is shown in Figure 12. For a higher thermal Biot number (Bi), both the concentration field and the thickness of the corresponding boundary layer are magnified.

Figure 13 shows $F(\zeta)$ for both cases, with and without (N_j). The plot shows that the flow is smooth everywhere in the geometry, but it speeds up significantly as the parameter increases. We see the effects on the concentration profile in Figures 14 and 15. Concentration boundary layer thickness decreases with the increase in Brownian motion parameter values; however, the thermophoresis parameter's effect on nanoparticle concentration follows the opposite trend.

The numerical results for many physical parameters are shown in Tables 2–4. These include the strength of the magnetic field, buoyancy ratio, Rayleigh number, radiation properties, Prandtl number, dimensionless reaction rate, non-dimensional activation energy, fitted rate constant, temperature gradient, thermophoresis effects, Schmidt number, Biot number, and convection-diffusion parameters. These factors directly impact the Sherwood number, Nusselt number, and skin friction coefficient. Notably, the skin friction and Nusselt numbers positively correlate with the magnetic field and buoyancy ratio parameters, while the activation energy and Sherwood numbers show an inverse relationship.

5 Conclusion

We have extensively analyzed the convective boundary conditions in a horizontal channel for Couette-Poiseuille MHD radiative heat and mass transfer. Our analysis incorporates the Buongiorno model, activation energy, chemical processes, and concentration fields. We do a thorough analysis that considers Joule heating, viscosity dissipation, radiation, and energy distribution. By utilizing an appropriate similarity transformation, we have converted the flow issue into a form that lacks dimensions and efficiently employed the Haar Wavelet Collocation approach to solve it. The graphical depictions of diverse, dynamic variables for nanofluid have been clarified. The main discoveries from our investigation demonstrate several essential observations.

The magnetic field parameter substantially influences the distribution of heat and mass, causing a corresponding impact on the flow field. An increase in the magnetic parameter leads to a decrease in the velocity of the nanofluid. Heat and mass distribution behavior during a chemical process shows unexpected patterns. The shear effects on both walls produce contrasting effects on the buoyancy ratio and magnetic parameter, and the heat transfer effects on both walls intensify with an unspecified factor. These discoveries enhance our comprehension of the intricate interconnections within this system and provide useful perspectives for future research in this subject.

Acknowledgments: The author would like to extend his sincere appreciation to the Researchers Supporting Project number (RSPD2023R920), King Saud University, Saudi Arabia.

Funding information: The Researchers Supporting Project number (RSPD2023R920), King Saud University, Saudi Arabia.

Author contributions: The author has accepted responsibility for the entire content of this manuscript and approved its submission.

Conflict of interest: The author states no conflict of interest.

References

[1] Choi S. Enhancing thermal conductivity of fluids with nanoparticle. In: Siginer DA, Wang HP, editors. Developments and applications of non-Newtonian flows. Vol. 66. New York: American Society of Mathematical Engineers; 1995. p. 99–105.

[2] Lee S, Choi SUS, Eastman JA. Measuring thermal conductivity of fluids containing oxide nanoparticles. J Heat Transf. 1999;121:280–9.

[3] Lyu X, Wang X, Qi C, Sun R. Characteristics of cavity dynamics, forces, and trajectories on vertical water entries with two spheres side-by-side. Phys Fluids. 2023;35(9):92101. doi: 10.1063/5.0166794.

[4] Makinde OD, Aziz A. Boundary layer flow of a nanofluid past a stretching sheet with a convective boundary condition. Int J Therm Sci. 2011;50:1326–32.

[5] Ellahi R, Aziz S, Zeeshan A. Non-Newtonian nanofluids flow through a porous medium between two coaxial cylinders with heat transfer and variable viscosity. J Porous Media. 2013;16:205–16.
[6] Kuznetsov AV, Nield DA. Natural convective boundary layer flow of a nanofluid past a vertical plate. Int J Therm Sci. 2010;49:243–7.
[7] Buongiorno J. Convective transport in nanofluids. J Heat Transf. 2006;128:240–50.
[8] Wang Z, Wang Q, Jia C, Bai J. Thermal evolution of chemical structure and mechanism of oil sands bitumen. Energy (Oxford). 2022;244:1. doi: 10.1016/j.energy.2022.123190.
[9] Zheng B, Lin D, Qi S, Hu Y, Jin Y, Chen Q, et al. Turbulent skin-friction drag reduction by annular dielectric barrier discharge plasma actuator. Phys Fluids. 2023;35(12):125129. doi: 10.1063/5.0172381.
[10] Das SK, Choi SU, Patel HE. Heat transfer in nanofluids—a review. Heat Transf Eng. 2006 Dec;27(10):3–19.
[11] Hu G, Ying S, Qi H, Yu L, Li G. Design, analysis and optimization of a hybrid fluid flow magnetorheological damper based on multiphysics coupling model. Mech Syst Signal Process. 2023;205:110877. doi: 10.1016/j.ymssp.2023.110877.
[12] Nimmy P, Nagaraja KV, Pudhari Srilatha K, Karthik G, Sowmya RS, Varun Kumar U, et al. Implication of radiation on the thermal behavior of a partially wetted dovetail fin using an artificial neural network. Case Stud Therm Eng. 2023;51:103552.
[13] Parvin S, Isa SSPM, Al-Duais FS, Hussain SM, Jamshed W, Safdar R, et al. The flow, thermal, and mass properties of Soret-Dufour model of magnetized maxwell nanofluid flow over a shrinkage inclined surface. PLoS One. 17(4):e0267148.
[14] Hayat T, Yasmin H, Ahmad B, Chen GQ. Exact solution for peristaltic transport of a micropolar fluid in a channel with convective boundary conditions and heat source/sink. Z Naturforsch A. 2014;69(8–9):425–32.
[15] Hussain SM, Khan U, Zaib A, Ishak A, Sarris IE. Numerical computation of mixed convective entropy optimized in Darcy-Forchheimer flow of cross nanofluids through a vertical flat plate with irregular heat source/sink. Tribol Int. 2023;187:108757.
[16] Yasmin H, Iqbal N, Tanveer A. Engineering applications of peristaltic fluid flow with Hall current, thermal deposition, and convective conditions. Mathematics. 2020;8(10):171.
[17] Hayat T, Iqbal M, Yasmin H, Alsaadi FE, Gao H. Simultaneous effects of Hall and convective conditions on peristaltic flow of couple-stress fluid in an inclined asymmetric channel. Pramana. 2015;85(1):125–48.
[18] Hayat T, Anwar MS, Farooq M, Alsaedi A. Mixed convection flow of viscoelastic fluid by a stretching cylinder with heat transfer. PLoS One. 2015;10:118815.
[19] Abbasi FM, Shehzad SA, Hayat T, Ahmad B. Doubly stratified mixed convection flow of maxwell nanofluid with heat generation/absorption. J Magn Magn Mater. 2016;404:159–65.
[20] Das K. Slip effects on MHD mixed convection stagnation point flow of a micropolar fluid towards a shrinking vertical sheet. Comput Math Appl. 2012;63:255–67.
[21] Hayat T, Waqas M, Shehzad SA, Alsaedi A. Mixed convection radiative flow of Maxwell fluid near a stagnation point with convective condition. J Mech. 2013;29:403–9.
[22] Rana S, Tabassum R, Mehmood R, Tag-eldin EM. Influence of Hall current & Lorentz force with nonlinear thermal radiation in an inclined slip flow of couple stress fluid over a Riga plate. Ain Shams Eng J. 2024;15(1):102319.
[23] Lou Q, Ali B, Rehman SU, Habib D, Abdal S, Shah NA. Micropolar dusty fluid: Coriolis force effects on dynamics of MHD rotating fluid when Lorentz force is significant. Mathematics. 2022;10:2630.
[24] Mukhtar S, Noor S. The numerical investigation of a fractional-order multi-dimensional model of Navier–Stokes equation via novel techniques. Symmetry. 2022;14(6):1102.
[25] Saad Alshehry A, Imran M, Khan A, Weera W. Fractional view analysis of Kuramoto–Sivashinsky equations with non-singular Kernel operators. Symmetry. 2022;14(7):1463.
[26] Sajid T, Sagheer M, Hussain S, Bilal M. Darcy-Forchheimer flow of Maxwell nanofluid flow with nonlinear thermal radiation and activation energy. AIP Adv. 2018;8(3):035102.
[27] Botmart T, Agarwal RP, Naeem M, Khan A. On the solution of fractional modified Boussinesq and approximate long wave equations with non-singular Kernel operators. AIMS Math. 2022;7:12483–513.
[28] Shahzad H, Ain QU, Ali A, Irshad K, Ali Shah I, Ghaffari A, et al. Double-diffusive natural convection energy transfer in magnetically influenced Casson fluid flow in trapezoidal enclosure with fillets. Int Commun Heat Mass Transf. 2022;137:106236.
[29] Yasmin H, Aljahdaly NH, Saeed AM, Shah R. Probing families of optical soliton solutions in fractional perturbed Radhakrishnan–Kundu–Lakshmanan model with improved versions of extended direct algebraic method. Fractal Fract. 2023;7(7):512.
[30] Shahid A, Huang HL, Bhatti MM, Marin M. Numerical computation of magnetized bioconvection nanofluid flow with temperature-dependent viscosity and Arrhenius kinetic. Math Comput Simul. 2022;200:377–92.
[31] Yasmin H, Aljahdaly NH, Saeed AM, Shah R. Investigating families of Soliton solutions for the complex structured coupled fractional Biswas–Arshed model in birefringent fibers using a novel analytical technique. Fractal Fract. 2023;7(7):491.
[32] Bestman AR. Natural convection boundary layer with suction and mass transfer in a porous medium. Int J Energy Res. 1990;14:389–96.
[33] Maleque K. Effects of binary chemical reaction and activation energy on MHD boundary layer heat and mass transfer flow with viscous dissipation and heat generation/absorption. ISRN Thermodyn. 2013;2013:284637.
[34] Mustafa M, Hayat T, Obaidat S. Boundary layer flow of a nanofluid over an exponentially stretching sheet with convective boundary conditions. Int J Numer Methods Heat Fluid Flow. 2013;23:945–59.
[35] Mohyud-Din ST, Khan U, Ahmed N, Bin-Mohsin B. Heat and mass transfer analysis for MHD model. Neural Comput Appl. 2017;28:4079–92.
[36] Awad FG, Motsa S, Khumalo M. Heat and mass transfer in unsteady rotating fluid flow with binary chemical reaction and activation energy. PLoS One. 2014;9:e107622.
[37] Shafique Z, Mustafa M, Mushtaq A. Boundary layer flow of Maxwell fluid in rotating frame with binary chemical reaction and activation energy. Results Phys. 2016;6:627–33.
[38] Lepik U. Haar Wavelet method for non-linear integro-differential equations. Appl Math Comput. 2006;176:324–33. doi: 10.1016/j.amc.2005.09.080.
[39] Lepik U. Numerical solution of evolution equations by the Haar Wavelet method. Appl Math Comput. 2007;185:695–704. doi: 10.1016/j.amc.2006.07.101.

[40] Islam SU, Sarler B, Aziz I, Haq F. Haar Wavelet collocation method for the numerical solution of boundary layer fluid flow problems. Therm Sci. 2011;50:686–97.
[41] Mustafa M, Khan JA, Hayat T, Alsaedi A. Buoyancy effects on the MHD nanofluid flow past a vertical surface with chemical reaction and activation energy. Int J Heat Mass Transf. 2017;108:1340–6.
[42] Revnic C, Grosan T, Pop I, Ingham DB. Magnetic field effect on the unsteady free convection flow in a square cavity filled with a porous medium with a constant heat generation. Int J Heat Mass Transf. 2011;54:1734–42.
[43] Tencer M, Moss JS, Zapach T. Arrhenius average temperature: The effective temperature for non-fatigue wear out and long-term reliability in variable thermal conditions and climates. IEEE Trans Compon Packag Technol. 2004;27:602–7.
[44] Kuznetsov AV, Nield DA. Natural convective boundary-layer flow of a nanofluid past a vertical plate. Int J Therm Sci. 2010;49:243–7.
[45] Zhang C, Zheng L, Zhang X, Chen G. MHD flow and radiation heat transfer of nanofluids in porous media with variable surface heat flux and chemical reaction. Appl Math Model. 2015;39:165–81.